AGU PUBLICATIONS

JGR

Journal of Geophysical Research: Space Physics

RESEARCH ARTICLE

10.1002/2014JA020703

Key Points:
- Local plasma densities and magnetic fields are measured by MARSIS onboard MEX
- Crustal magnetic fields influence the configuration of the ionosphere
- Densities are elevated over regions where the crustal field dominates

Correspondence to:
D. J. Andrews,
david.andrews@irfu.se

Citation:
Andrews, D. J., N. J. T. Edberg, A. I. Eriksson, D. A. Gurnett, D. Morgan, F. Němec, and H. J. Opgenoorth (2015), Control of the topside Martian ionosphere by crustal magnetic fields, *J. Geophys. Res. Space Physics*, *120*, 3042–3058, doi:10.1002/2014JA020703.

Received 8 OCT 2014
Accepted 4 MAR 2015
Accepted article online 10 MAR 2015
Published online 14 APR 2015

Control of the topside Martian ionosphere by crustal magnetic fields

D. J. Andrews[1], N. J. T. Edberg[1], A. I. Eriksson[1], D. A. Gurnett[2], D. Morgan[2], F. Němec[3], and H. J. Opgenoorth[1]

[1]Swedish Institute of Space Physics, Uppsala, Sweden, [2]Department of Physics and Astronomy, University of Iowa, Iowa City, Iowa, USA, [3]Faculty of Mathematics and Physics, Charles University in Prague, Prague, Czech Republic

Abstract We present observations from the Mars Advanced Radar for Subsurface and Ionospheric Sounding (MARSIS) instrument onboard Mars Express of the thermal electron plasma density of the Martian ionosphere and investigate the extent to which it is influenced by the presence of Mars's remnant crustal magnetic fields. We use locally measured electron densities, derived when MARSIS is operating in active ionospheric sounding (AIS) mode, covering an altitude range from ~300 km to ~1200 km. We compare these measured densities to an empirical model of the dayside ionospheric plasma density in this diffusive transport-dominated regime. We show that small spatial-scale departures from the averaged values are strongly correlated with the pattern of the crustal fields. Persistently elevated densities are seen in regions of relatively stronger crustal fields across the whole altitude range. Comparing these results with measurements of the (scalar) magnetic field also obtained by MARSIS/AIS, we characterize the dayside strength of the draped magnetic fields in the same regions. Finally, we provide a revised empirical model of the plasma density in the Martian ionosphere, including parameterizations for both the crustal field-dominated and draping-dominated regimes.

1. Introduction

The Martian ionosphere is formed principally through the photo-ionization of its CO_2-dominated neutral atmosphere, and the main layer is reasonably well approximated by a Chapman layer, with peak subsolar electron densities of the order of $\sim 1.5 \times 10^5$ cm^{-3} at altitude of ~130 km [see, e.g., *Nagy et al.*, 2004; *Witasse et al.*, 2008; *Withers*, 2009; *Haider et al.*, 2011, and references therein]. This conducting ionosphere is a direct obstacle to the impinging supersonic solar wind, and a dynamic interaction region is established in which a bow shock (BS) is formed, below which the solar wind is slowed to subsonic speeds and heated to form the magnetosheath. A second clear boundary, termed the magnetic pileup boundary (MPB), is found below the magnetosheath and marks a significant change in the magnetic field strength as the interplanetary magnetic field (IMF) is "piled up" during its convection around and through the upper reaches of the ionospheric obstacle. Inside the MPB, the variability of the magnetic field also typically decreases [*Acuña et al.*, 1998].

While the interaction between the impinging solar wind the Martian ionosphere shares many characteristics of the somewhat similar interactions found at Venus and Titan in particular, the presence of significant crustal magnetic fields unique to Mars introduces additional complexities. These crustal fields, first detected in Mars Global Surveyor magnetometer data [*Acuña et al.*, 1998] and later extensively surveyed, are distributed over much of the Martian surface but are most intense at southern latitudes near ~180° east longitude [*Acuña et al.*, 1999, 2001; *Connerney et al.*, 1999, 2001]. Subsequently, various numerical schemes have been used to describe the spatial dependence of these crustal fields [e.g., *Purucker et al.*, 2000; *Arkani-Hamed*, 2001, 2004; *Cain et al.*, 2003; *Lillis et al.*, 2010; *Morschhauser et al.*, 2014]. Below ~500 km altitude these crustal fields are frequently more intense than that typical of the draped IMF, and thus, they markedly affect various aspects of the ionosphere. Strong evidence exists for significant modifications of the dayside ionosphere in regions of intense near-vertical crustal fields, where localized ionospheric upwellings have been inferred from the detection of oblique radio reflections in sounding data [*Gurnett et al.*, 2005; *Duru et al.*, 2006; *Nielsen et al.*, 2007; *Andrews et al.*, 2014].

Initial evidence has also been presented for the influence of crustal magnetic fields on the ionospheric plasma density configuration at altitudes above ~250 km, where the characteristic timescales of photochemical processes are significantly longer than diffusive transport timescales (i.e., the equilibrium

configuration is established through a balance in transport processes). Recent studies have addressed the influence of crustal fields on the ionospheric ions with thermal energies, using measurements made by both the Analyzer for Space Plasmas and Energetic Atoms (ASPERA-3) and Mars Advanced Radar for Subsurface and Ionospheric Sounding (MARSIS) instruments onboard European Space Agency (ESA)'s Mars Express (MEX) spacecraft [*Barabash et al.*, 2006; *Picardi et al.*, 2004; *Chicarro et al.*, 2004]. *Nilsson et al.* [2011] computed ion fluxes from ~5000 orbits of ASPERA-3 ion data, finding enhanced net escape fluxes of planetary ions at high altitudes (greater than ~1000 km or ~0.2 R_M) above the northern hemisphere of Mars, where crustal fields are typically weaker (Mars' equatorial radius $R_M = 3396$ km). Conversely, ion fluxes at low altitudes in the southern hemisphere (with generally stronger crustal fields) were enhanced relative to the same altitude range in the northern hemisphere, consistent with similar studies of these data performed by *Dubinin et al.* [2012] and *Lundin et al.* [2013]. A consensus therefore is emerging which suggests that under present-day conditions, the integrated effect of these crustal fields is to locally reduce the escaping fluxes of ionospheric plasma, though the mechanism by which this occurs is poorly constrained by the available observations. More recently, *Andrews et al.* [2013] showed for the first time using in situ measurements of ionospheric electron density that the crustal fields exerted a measurable influence on the configuration of the ionosphere, at altitudes well above the ionospheric peak. In addition, both the BS and the MPB have been shown (statistically) to be located at higher altitudes over regions where the crustal fields are more intense [*Crider et al.*, 2002; *Edberg et al.*, 2008, 2009].

Various modeling studies have sought to develop understanding of the effects of the crustal fields on the Martian ionosphere and induced magnetosphere. High-resolution magnetohydrodynamic models have been developed, and the inclusion of static (nonrotating) crustal fields within these models has been shown to have an effect on the configuration of the ionosphere, induced magnetosphere, and, ultimately, the rate of escaping ionospheric plasma [*Ma et al.*, 2002, 2004; *Ma and Nagy*, 2007; *Ma et al.*, 2014; *Najib et al.*, 2011; *Dong et al.*, 2014; *Harnett and Winglee*, 2003, 2005, 2007]. The high spatial resolution required to include an accurate representation of the crustal fields has thus far restricted their use in hybrid models, though an initial estimate of their role in modulation ionospheric outflow has been performed [*Brecht and Ledvina*, 2014].

In this paper, we further examine the relationship between these crustal fields and the Martian ionospheric plasma, by studying the spatial dependence of increases and decreases in the observed plasma density with respect to an empirical model. This allows us to make comparisons on smaller scales than have been made previously, revealing the ionospheric role of the crustal fields in new detail.

2. Instrumentation

In this paper we use data from the MARSIS instrument, which is typically operated for ~20 min before and after periapsis on each ~7 h MEX orbit, corresponding to spacecraft altitudes between ~300 and ~1200 km. MARSIS has two separate modes of operation: a "subsurface" (SS) mode and an "Active Ionospheric Sounding" (AIS) mode. Particularly over the nightside, the SS mode is operated for the majority of MEX periapsis passes and the only ionospheric products obtained are measurements of the vertically integrated electron column density, which are dominated by the low-altitude ionosphere near its peak density at ~135 km altitude, and are therefore not used in this study. During AIS mode operations, a powerful ~100 μs radio pulse with central frequency f_s is transmitted on the antenna, which is specularly reflected from the ionosphere at the altitude at which it encounters a plasma of sufficient density that the pulse no longer propagates. The instrument records any such reflections received over ~7.5 ms following the transmission of the pulse, before repeating the same process with a higher-frequency pulse. The ~7.5 ms period for which the instrument is "listening" is divided into 80 separate intervals each of ~91 μs duration. In total, within each sounding, 160 distinct pulses with central frequencies quasi-logarithmically spaced from ~100 kHz to ~5.5 MHz are transmitted. One such sounding is performed every ~7.5 s.

Two examples of the data recorded are shown in Figure 1, presented as so-called "ionograms," in which the accumulated signal on the radar is shown color coded versus both the sounding frequency f_s and the elapsed time from the initial pulse transmission τ_D. Both soundings were performed on the same periapsis segment of orbit 3058 on 28 May 2006 (used previously for purposes of exposition by *Gurnett et al.* [2008]). The first was taken at a solar zenith angle χ of 82° and an altitude of 480 km, while the second was taken at $\chi = 60°$ and an altitude of ~370 km. In both cases a clear reflection from the Martian topside ionosphere is

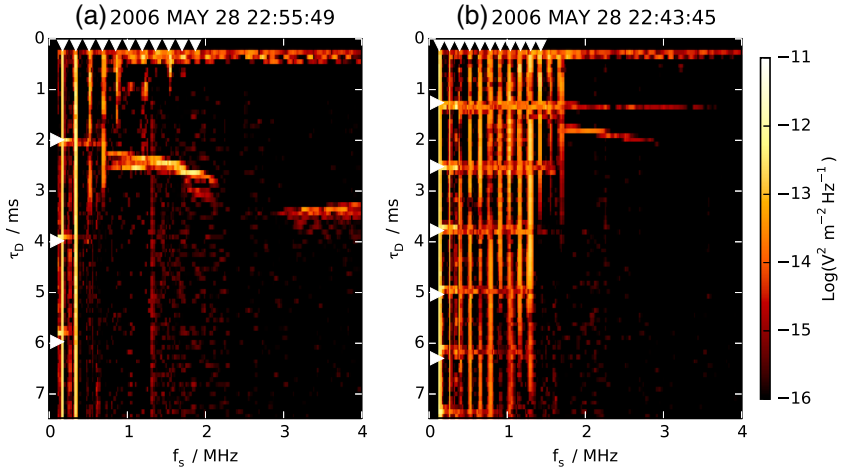

Figure 1. Two example ionograms taken with MARSIS AIS at two points on orbit 3058, on 28 May 2006. Signal intensity is color coded as a function of both the sounding frequency f_s and delay time τ_D. The fitted series of plasma lines nf_{pe} is indicated by the downward pointing triangles on the upper edge of the plot. Similarly, fitted electron gyroperiod pseudoechoes are indicated by the right-facing triangles on the left edge of each plot. Clear ionospheric reflections are also visible between (a) ~0.8 and ~2 MHz and (b) ~1.7 to ~2.9 MHz. A clear surface reflection is also present in Figure 1a at and above ~3 MHz

visible as the continuous trace, from ~0.8 to ~2 MHz in Figure 1a and from ~1.7 to ~2.9 MHz in Figure 1b. The curve formed by the measured delay τ_D between the transmission and the reception of the reflection as a function of increasing pulse frequency can be numerically inverted to form a vertical profile of the topside ionospheric electron density [*Morgan et al.*, 2013]. In the first ionogram, a clear surface reflection is also detected above ~2.9 MHz. In addition to these reflections, a variety of other signals are present in the ionograms, chief among which are regularly spaced vertical lines at the local electron plasma frequency f_{pe}, and higher harmonics thereof produced by the instrument electronics. These are produced by the interaction of the intense sounding pulse with the local plasma medium and the processing of the antenna signal on board the spacecraft [*Gurnett et al.*, 2005; *Duru et al.*, 2008; *Morgan et al.*, 2013] and can be used to derive the local electron plasma density n_e through

$$n_e = \frac{\epsilon_0 m_e}{e^2}\left(2\pi f_{pe}\right)^2 \approx \left(\frac{f_{pe}}{8980}\right)^2, \quad (1)$$

in which n_e is expressed in units of cm^{-3}, f_{pe} is expressed in hertz, and the other symbols have their usual meanings and mks dimensions. We use the method described by *Andrews et al.* [2013] to process each ionogram, in which the absolute intensity of these plasma lines is used to guide an automatic method to yield consistently accurate results across the >3 orders of magnitude range in n_e typically encountered at these altitudes in the Martian ionosphere. The empirical method, calibrated through comparison with existing manually estimated values, has been shown to be sufficiently robust as to allow use of these data in large statistical studies [*Andrews et al.*, 2013]. The plasma frequencies determined by this automatic method (and the first 10 integer multiples thereof) are indicated by the white triangles on the upper axis of each panel in Figure 1. The derived local plasma densities n_e are ~360 cm^{-3} and ~210 cm^{-3} for the cases shown in Figures 1a and 1b, and the corresponding marked positions can be seen to be in good agreement with the observed local plasma frequency lines, where they are clearly visible in the data. The number of harmonic plasma lines observed is related both to the spacing between adjacent sounding frequencies, which is nonlinear, and variations in the instrument gain with frequency [*Jordan et al.*, 2009].

Somewhat similarly, apparent echoes are also often observed in AIS soundings, at delays that correspond to the local electron gyroperiod, and its harmonics. These appear as regularly spaced horizontal traces within the ionograms, with the spacing being the local electron gyroperiod τ_{ce} where

$$\tau_{ce} = \frac{2\pi m_e}{e|B|}. \quad (2)$$

By locating these gyroperiod "pseudoreflections" the local scalar magnetic field strength can be derived, providing it lies in the range ~5 to ~200 nT, as is typically the case at these altitudes in the Martian system. Each AIS sounding is again automatically inspected, and a simplified version of the same technique used in determining the plasma density is applied to compute the electron gyroperiod from these apparent echoes, yielding a measurement of $|B|$ (This related technique again involves applying the same threshold to the ionogram "image," before extracting those horizontal features which are continuous over the lower sounding frequencies and determining their widths and spacings.). The accuracy of this measurement is constrained in part by the temporal resolution with which MARSIS AIS measures the intervening time between the transmission of pulses and the reception of any reflections, and the fact that the determined value of $|B|$ is the reciprocal of the measured delay. This corresponds to a minimum uncertainty of ~1% in the weakest fields that can be measured and increasing as $\tau_D^{1/2}$ to ~35% in the strongest fields. The length of time following the pulse transmission for which AIS is able to measure a signal from $\tau_D = 0.25$ to 7.5 ms, and is grouped into 80 distinct intervals of identical size. This constrains the ability of the electron gyroperiod to be resolved to regimes for which $|B|$ is greater than ~5 nT (corresponding to a cyclotron pseudoecho observed in the last delay interval sampled) and less than ~200 nT (corresponding to the Nyquist frequency of the sampled delays). Fortuitously, within the ~300 to ~1200 km altitudes where these measurements are made, this is sufficient range for all but the most extreme conditions experienced thus far in the Martian-induced magnetosphere [cf. *Brain et al.*, 2003; *Crider et al.*, 2004, 2005].

Applying this method to the ionograms shown in Figures 1a and 1b, the resulting values of $|B|$ are ~20 nT and ~28 nT, respectively. Once again, equivalent values of τ_{ce} and its harmonics are shown by the automatically determined white icons on the left-hand axis of each figure. Within these two examples, a mild bias of the technique to fitting the first observed cyclotron pseudoecho is apparent (a consequence of this first line typically being the strongest observed and extending over the widest range of sounding frequency f_s). Combined with the relatively poorer resolution of this measurement compared to the determination of the local plasma density, this results in a measurement of $|B|$ that is substantially less accurate than a properly designed and calibrated magnetometer but is nevertheless sufficient to resolve typical crustal and induced magnetic fields in the Martian system.

3. Observations

3.1. The *Němec et al.* [2011] Model

In this section we first present the *Němec et al.* [2011] model of the Martian upper ionosphere, herein after referred to as the *N11* model. The N11 model is a complete empirical specification of the Martian ionospheric electron density, comprised through fits to MARSIS data obtained during the period August 2005 to the end of 2009. The model conveniently describes topside plasma density measurements determined both via numerical inversion of ionospheric reflection traces, such as those noted in Figure 1, in addition to in situ measurements made via (manually) processing the same plasma frequency oscillations that are later studied in this paper. Near the peak, the model uses simple Chapman theory to describe the ionosphere in terms of a peak density, scale height, and the dependence of these parameters on the flux of ionizing radiation that the atmosphere is exposed to (dependant both on the state of the Sun, as approximated through the $F_{10.7}$ index of solar radio emission, and the Mars-Sun distance). Here we summarize the characteristics of the N11 model as it pertains to the altitudes sampled in situ by MEX, well above the ionospheric peak. Here the model specifies the equilibrium density $n_e(h, \chi)$ which is established through plasma diffusion,

$$n_e(h, \chi) = n_0(\chi) \exp\left(\frac{-(h - h_0)}{H(\chi)}\right), \tag{3a}$$

where

$$n_0(\chi) = \begin{cases} 2800\ \text{cm}^{-3} & \chi < 70° \\ 6530\ \text{cm}^{-3} - 57\ \text{cm}^{-3}\ \text{deg}^{-1} \cdot \chi, & 70° < \chi < 100°, \end{cases} \tag{3b}$$

and

$$H(\chi) = 781\ \text{km} \cdot \sin\left(\arctan\left(\frac{3\ \text{nT}}{40\ \text{nT} - 0.3\ \text{nT deg}^{-1} \cdot \chi}\right)\right). \tag{3c}$$

The electron densities n_e and n_0 are expressed in units of cm^{-3}, altitude h and scale height H in kilometers, and solar zenith angle χ in degrees, with the dimensions of the numerical constants as appropriate, having

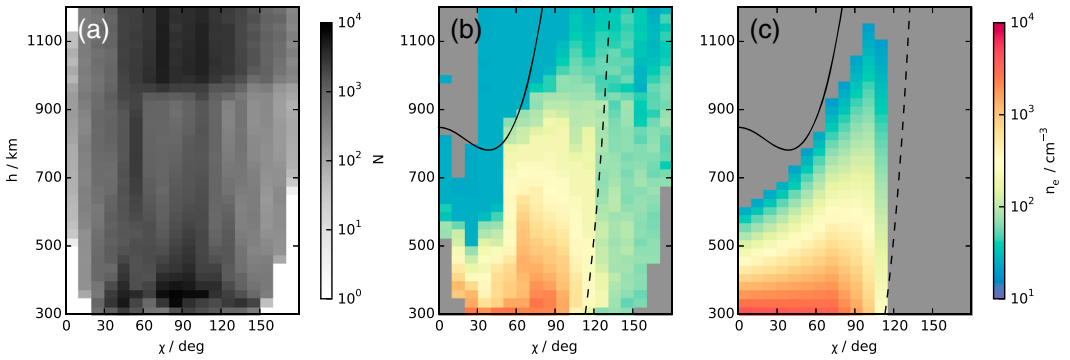

Figure 2. (a) Number of MARSIS AIS data points recorded, binned by altitude h and solar zenith angle χ. (b) Median measured thermal electron densities measured within each bin, using the method described by *Andrews et al.* [2013]. Grey coloring indicates those regions where insufficient measurements of the local plasma frequency have been recorded. (c) The N11 model of the Martian dayside ionosphere. Grey coloring here indicates model densities below the range that can be reliably measured with MARSIS.

been determined by fits to a subset of the available AIS data, as described in detail by N11. The arbitrary reference altitude $h_0 = 325$ km.

The model is appropriate to the upper reaches of the Martian ionosphere, in which the configuration is determined by diffusive processes, which leads to a simple exponential decrease in density with altitude. More specifically, this transition to a diffusion-dominated density structure takes place ~5–10 scale heights above the ionospheric peak and is well established at the upper bound of that range, equivalent to altitudes h above ~250 km at the subsolar point (~300 km at $\chi = 75°$). Meanwhile, the functional form of $H(\chi)$ is obtained through the consideration of the reduction of the efficiency of vertical diffusion by the presence of a draped magnetospheric field. To first order, this reduces the vertical scale height by a factor sin I, where I is the inclination of the field with respect to the surface, $I = \arctan(B_r/B_h)$ in which B_r and B_h are, respectively, the radial and horizontal components of the draped field. The geometry of the draped field, as expressed in equation (3c) is derived from analysis of Mars Global Surveyor (MGS) magnetometer data by *Brain et al.* [2003]. In this respect, the model is constrained by observations up to $\chi \approx 100°$, although the effects of changing solar illumination and Martian season are not included, and is strictly only valid within a narrow range of local time centered on the 0200–1400 h plane containing the MGS orbit. We note that while the N11 model includes expressions that modify the plasma density at lower altitudes according to the instantaneous value of the $F_{10.7}$ index, it makes no account for similar effects at the higher altitudes which we study in this paper. However, the large available data set, spanning more than four Martian years and a large fraction of a solar cycle significantly mitigates this effect, at least when studying the larger-scale aspects of the system in a statistical manner.

In Figure 2 we show densities derived from the MARSIS/AIS instrument, as described by *Andrews et al.* [2013]. In this and the following figures, the data shown were taken during the period November 2005 (after which the AIS sounding frequency table has remained fixed) to August 2014, and total ~1.1 million records. For reference, in each panel of Figure 2 we overplot both the modeled position of the magnetic pileup boundary (MPB, solid black line) as determined by *Trotignon et al.* [2006], and the terminator (dashed black line). We note that this model of the MPB, as with all others currently in existence, is not well constrained at low solar zenith angles due to a lack of observed MPB crossings in this region. Figure 2a shows the available number of discrete measurements N, each corresponding to a single AIS sounding, recorded within bins of 10° in χ, and 25 km in h, from which it can be seen that reasonable sampling in χ is achieved at all altitudes, and only the very deep nightside at low altitudes remains unexplored. The moderately increased volume of AIS data available above ~950 km is a consequence of the more frequent operation of the counterpart subsurface sounding mode below this altitude. Figure 2b shows the median in situ electron density recorded in each bin for which at least 20 separate measurements of the local plasma density were determined (therefore requiring at least 20 separate soundings to have been performed in the corresponding region, cf. Figure 2a). Nondeterminations of the plasma density correspond to situations in which either a sounding was performed while MEX was located in the hot, fast-flowing plasma of the Martian magnetosheath, or the local plasma density was, in fact, sufficiently low (n_e below ~20 cm^{-3}) such

that the harmonics of the plasma oscillations were effectively inseparable, forming a "continuum" within the ionogram [*Duru et al.*, 2008; *Andrews et al.*, 2013]. Finally, Figure 2c shows densities n_e obtained from the N11 model, evaluated on the same grid of h and χ and using the same color scale as that for Figure 2b such that direct comparisons can be made.

A reasonable correspondence exists between the observed plasma densities shown in Figure 2b and those obtained from the N11 model on the dayside, both in terms of absolute values and vertical gradients in the density. Similarly, the same trend of increasing densities with increasing χ at fixed altitudes is apparent in both Figures 2b and 2c, up to a χ of ~90°. The scale height H of the N11 model ranges from ~60 km at $\chi = 0°$ up to ~180 km at $\chi = 90°$, with measured variations about these values being of the order of ~50 km. It is noted, however, that the observed densities do depart from those described by the model at the highest altitudes shown—median plasma densities typically exceed values of a few tens of cm^{-3} throughout those regions where measurements are available, yet the corresponding modeled values are often insignificant, e.g., at low χ and high altitudes. This apparent discrepancy may result from a somewhat different treatment of those MARSIS soundings for which no plasma lines can be determined (which are subsequently excluded in our analysis but set to a zero value of density by N11).

In the following section we use the N11 model as a smoothly varying "baseline" to compare against observations, determining the relative difference between the densities predicted by the model and those measured. We then study the spatial dependence of the measured plasma densities in planetocentric coordinates, by comparing instantaneously measured values with average values determined in restricted altitude ranges, in order to examine their relationship to the Martian crustal magnetic fields.

3.2. Localized Density Variations at 350–400 km Altitude

In Figure 3 we show the distribution of magnetic fields and relative departures from the N11 model determined in the altitude range 350 to 400 km, in the dayside ionosphere ($\chi < 90°$). Figure 3a shows the magnitude $|B|$ of the crustal magnetic field at the lower bound of this altitude range, computed using the *Cain et al.* [2003] model. Note that in this and the following panels we show more than one complete cycle of longitude, such that the spatial variation of the crustal fields can be viewed continuously across the whole range. It should also be noted that owing to the orbital period of MEX being much shorter than the rotation period of the planet, the resulting sampling of longitude is highly uniform. While somewhat less optimal, the sampling in latitude is nevertheless sufficient at each altitude range studied that robust conclusions can be drawn, and no potential biases are present, particularly when the totality of the available data is considered. Figure 3b shows median values of $|B|$ derived from the MARSIS AIS data, through determinations of the local electron gyroperiod. Individual measurements of $|B|$ obtained with the 350 to 400 km altitude range are first binned according to the latitude and longitude of the observation, and the median value computed. As these data are taken on the dayside, the draped IMF strongly contributes to the measurements, through the addition of an approximately constant (quasi-uniform) field of ~30 nT to that of the crustal sources. In comparing the modeled field shown in Figure 3a and the measured values shown in Figure 3b, the most significant crustal feature that remains after the binning and averaging of the measured $|B|$ is the localized maximum centered in the southern hemisphere at ~180°. This indicates that the crustal fields at this location are often significantly stronger than the draped IMF at these altitudes, consistent with previous observations in similar data sets [e.g., *Brain et al.*, 2003].

In Figure 3c we examine the median differences between ionospheric electron densities derived from MARSIS AIS data and the N11 model, binned using the same spatial scheme as in Figure 3b. Specifically, for the N AIS soundings performed within a given bin, we compute the quantity

$$\Delta n_e = \frac{1}{N}\sum_{i=1}^{N} n_{e,i} - n_e(h_i, \chi_i), \tag{4}$$

where $n_{e,i}$ is the measured value of the local electron density determined from the ith ionogram, computed using the method of *Andrews et al.* [2013] from the AIS data, and $n_e(h_i, \chi_i)$ is the N11 model (equation (3)) evaluated at the spacecraft altitude h_i and solar zenith angle χ_i. The related dimensionless quantity,

$$V_{n_e} = \frac{1}{N}\sum_{i=1}^{N} \frac{n_{e,i} - \overline{n_{e,h}}}{\overline{n_{e,h}}}, \tag{5}$$

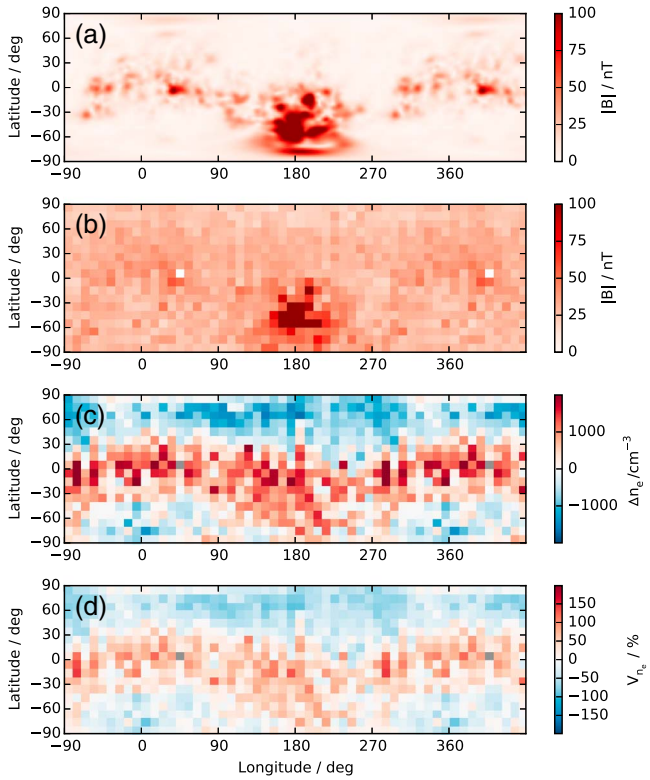

Figure 3. Magnetic fields and plasma densities measured in the Martian ionosphere within the altitude range 350 to 400 km. For clarity, we show an additional half cycle of longitude. (a) The magnetic field magnitude $|B|$ evaluated from the *Cain et al.* [2003] at 350 km altitude. (b) Measured averages of $|B|$ obtained from the local electron gyroperiod measurements made by MARSIS AIS, computed in 10° bins of latitude and longitude. (c) Mean relative differences Δn_e between plasma densities measured by MARSIS AIS using the method described by *Andrews et al.* [2013] and the model of N11, binned in the same latitude-longitude scheme as used in Figure 3b. Red colors indicate regions for which the measured plasma densities exceed the modeled value, and blue vice versa. (d) Relative differences V_{n_e} between local and averaged plasma densities measured with MARSIS AIS, expressed as a percentage. Again, red colors indicate densities above the average value for this altitude range, and blue vice versa. Gray coloring indicates those regions for which insufficient data were recorded to compute the quantities displayed.

is depicted in Figure 3d, where $\overline{n_{e,h}}$ is the measured plasma density within this altitude range averaged over both latitude and longitude. Expressed as a percentage, this shows the extent to which the measurement in a given small bin of latitude and longitude is elevated (or decreased) relative to the average at this altitude. Note that determined values of V_{n_e} can in principle exceed ±100%, representing a large departure from the average measured density at a given altitude. It is clearly apparent that these two quantities Δn_e and V_{n_e} are approximately proportional to one another, as a result of the only relatively weak variation in plasma density with both χ and h in this part of the ionosphere. As noted, typical scale heights in this region greatly exceed the 50 km vertical extent of the altitude range studied, while variations in plasma density with χ, as parameterized, for example, by the N11 model are small over most of the dayside ionosphere at these high altitudes. The color scales used for both Figures 3c and 3d are symmetric and centered on zero, such that positive values of Δn_e and V_{n_e} are shown red and negative values blue.

Examining first the density differences Δn_e shown in Figure 3c, a very clear organization of this parameter is immediately obvious, in that a continuous band of positive values of Δn_e is present, which very closely follows the similar banding present in the modeled crustal fields (shown in Figure 3a). This region of positive Δn_e, indicating measured densities that typically exceed the N11 model at the same location, has its largest latitudinal extent near 180° longitude, where it spans the entire southern hemisphere. Away from these longitudes, the band of positive Δn_e becomes more constrained in latitude but continues to closely follow the location of the most intense crustal field sources. Typical magnitudes of V_{n_e} (Figure 3d) seen in this region are ~0.4, reaching maximal values of ~2, indicating local densities which are significantly above the average values for this altitude range and that predicted by the N11 model. Outside of this band of positive V_{n_e}, observed values are typically negative, ~−0.2, indicating measured densities which are instead generally lower than the average values for this altitude range, to a broadly similar degree. Such a result is in itself unsurprising, as the N11 model represents the average conditions, independent of the crustal fields, and therefore, positive deviations from the model in one particular location should be approximately balanced by similar negative deviations elsewhere.

3.3. Altitude Ranges

We now extend the initial analysis presented in Figure 3 to a wider range of altitudes. In Figures 4 and 5 we show the departure between the measured and modeled plasma densities, and the measured magnetic

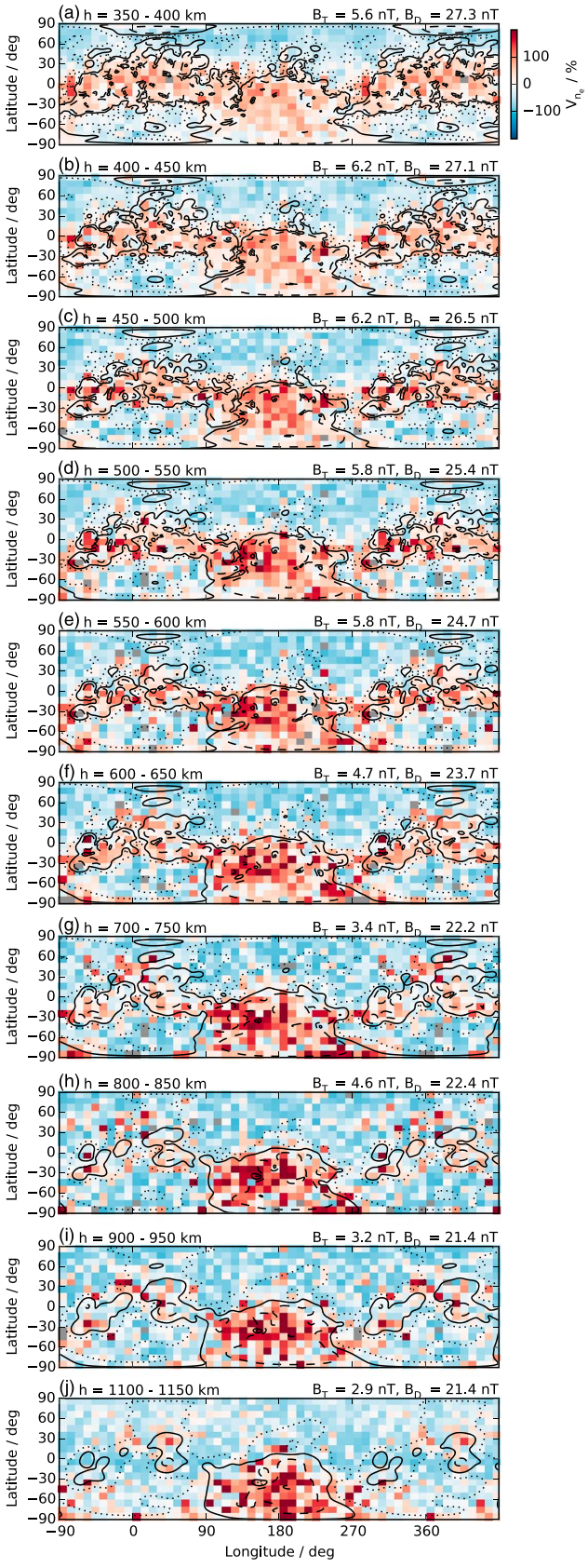

fields respectively, computed within 10 different ranges of altitude which span the extent sampled by AIS measurements. Figure 4 shows relative differences V_{n_e} computed on the same latitude and longitude grid used in Figure 3, in 10 increasing altitude ranges from $350 < h < 400$ km in Figure 3a to $1100 < h < 1150$ km in Figure 3j, each of 50 km vertical extent. The altitude range covered in each panel is indicated by the text at the upper left corner, and, for continuity, the data shown previously in Figure 3d are repeated in Figure 4a.

The same organization of the sense of V_{n_e} in this coordinate system noted in Figure 3 is clearly repeated throughout the other altitude ranges shown in Figure 4. At altitudes from 350 to 500 km (Figures 4a–4c), the elevation in measured plasma densities above their average values in regions of strong crustal fields is balanced, to some extent, by a similar-sized depletion in densities with respect to the average in regions of weaker crustal fields. In order to examine the extent to which the observed density differences V_{n_e} are controlled by the crustal fields, for each altitude range presented we show contours of the *Cain et al.* [2003] model, again computed at the lower boundary of each range. As the intensity of the crustal fields monotonically decreases with

Figure 4. (a–j) Relative differences V_{n_e} between measured and average plasma densities as computed for a range of increasing altitudes from $350 < h < 400$ km to $1100 < h < 1150$ km. Figure 4a shows, as a reference, the same altitude range depicted already in Figure 3c. The color scale used in each panel is identical to that given for Figure 4a. Gray coloring again indicates those regions for which insufficient data were recorded to compute the quantities displayed. The solid black contours in each plot are drawn where the *Cain et al.* [2003] model magnetic field at the depicted altitude B_{Cain} is equal to the determined threshold value B_T, itself computed from the structure of the plasma density variations shown, as described in the text. The determined value of B_T is and indicated in the upper right of each row, along with the determined value of the averaged draped magnetic field B_D. The dotted and dashed contours then represent $B_T/2$ and $2B_T$, respectively.

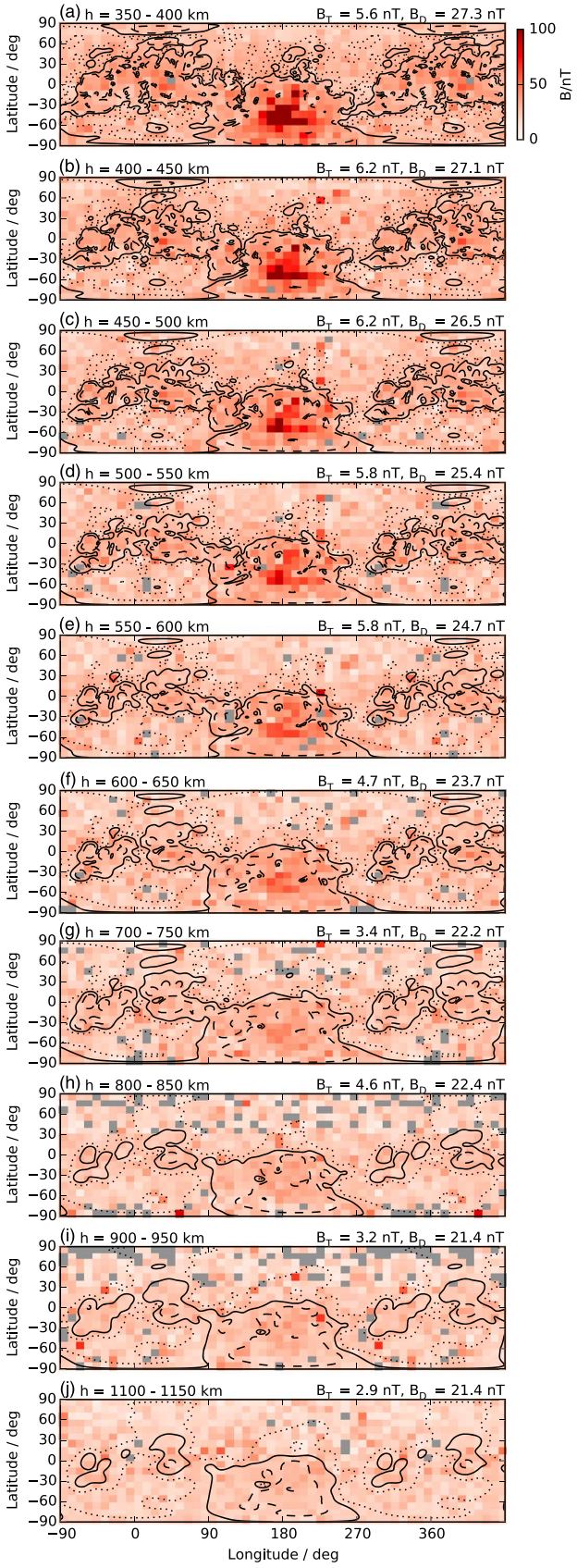

increasing altitude, we determine appropriate contours for each separate altitude range by determining a contour value B_T of the modeled magnetic field intensity, about which regions of positive values of V_{n_e} are most completely separated from those with negative values. The contour for which the *Cain et al.* [2003] model $|B_{\mathrm{Cain}}| = B_T$ is shown by the solid black line, while related contours at values of $B_T/2$ and $2B_T$ are shown by the dotted and dashed black lines, respectively. For each altitude range shown in Figure 4, the empirically determined value of B_T is indicated above the upper right corner and falls from ~6 nT at the lowest altitudes to ~3 nT at the highest sampled. By definition, therefore, a clear separation between regions of mainly positive and negative V_{n_e} can be seen to take place across the central contoured value of the modeled magnetic field B_T, although the "completeness" of the separation is clearly lower at higher altitudes. Quantitatively, ~80% of those bins for which V_{n_e} is of positive (negative) sign lie in the region for which $|B_{\mathrm{Cain}}|$ is greater (less) than B_T at the lowest altitudes studied (Figure 4a), while this fraction decreases to ~70% at the highest shown (Figure 4j).

The lack of a vector magnetometer onboard MEX precludes the separation of the observed field into crustal and noncrustal components, though it remains informative to compare the observed field magnitude with that of the crustal field as computed from a model. In Figure 5 we show median values of the magnetic field intensity, derived from MARSIS AIS measurements of the local electron gyroperiod and computed in the same altitude ranges and spatial bins used in

Figure 5. (a–j) Median measured dayside magnetic fields computed in the same altitude ranges used in Figure 4. Contours of the *Cain et al.* [2003] are again shown at $B_T/2$, B_T and $2B_T$ by the dotted, solid and dashed black lines. The color scale used is again identical in each panel, and gray coloring indicates bins for which insufficient data were available.

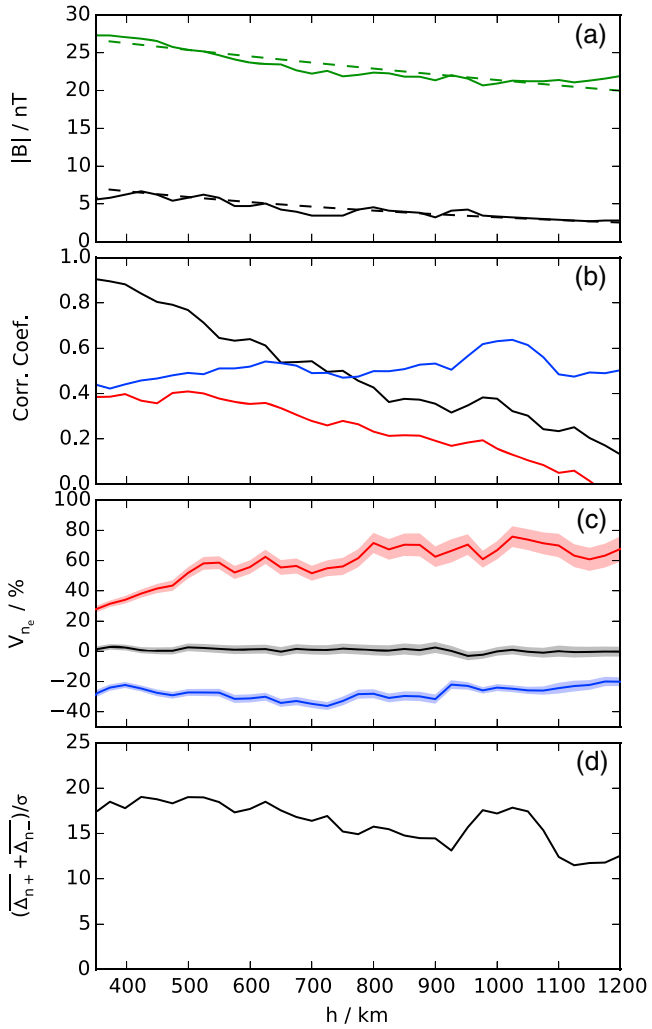

Figure 6. (a) B_T (solid black line) and B_D (solid green line) as a function of altitude. Exponential fits to each parameter are shown by the appropriately colored dashed lines. (b) Linear correlation coefficients as a function of altitude h. The black line shows the correlation between $|B|$ computed from the *Cain et al.* [2003] model and that observed by MARSIS AIS. The red line then shows the correlation between the observed values of $|B|$ and the relative density differences V_{n_e}. The blue line shows the correlation between $|B|$ computed from the *Cain et al.* [2003] model and V_{n_e}. (c) Mean values of V_{n_e} computed where the modeled value of $|B|$ is, respectively, greater than B_T (red line), less than B_T (blue line), and all available data (black line). Shaded regions of the appropriate color indicate the extent of the standard error on the mean value in each case. (d) Difference between values of V_{n_e} recorded in the stronger field region and in the weaker field region (red and blue lines in Figure 6c), scaled by the combined standard deviation in the measured values from which they are computed.

Figure 4. As previously, we consider only measurements made on the dayside and show again in Figure 5a the same data shown previously in Figure 3b. The same contoured values B_T of the *Cain et al.* [2003] model shown in Figure 4 are overplotted in each panel of Figure 5. At the lowest altitudes studied, measured magnetic field intensities are clearly comparable to those expected from the *Cain et al.* [2003] model in regions where the crustal fields are sufficiently strong as to dominate any draped IMF at the same location. A clear maximum in the measured values of $|B|$ remains visible centered near 180° east longitude in the southern hemisphere at all altitudes up to ~750 km (Figure 5g). At altitudes h above ~800 km (Figures 5h–5j), the measured mean fields are essentially independent of location over the surface; i.e., no crustal field signatures can be statistically identified in the available data, as binned in this manner. We somewhat crudely estimate the typical intensities of the draped IMF, B_D, by computing the mean value of $|B|$ as measured in regions where the crustal field is sufficiently weak (e.g., outside the dotted contour in each panel). Determined values of B_D within each altitude range are also indicated to the upper right of each panel in Figures 4 and 5.

In Figure 6 we quantitatively examine the variations in these measured plasma densities and measured fields versus altitude. The solid black line in Figure 6a shows the computed threshold value B_T of the *Cain et al.* [2003] field model as a function of altitude h. Here we show values of B_T computed in altitude ranges of 50 km height and spaced at 25 km intervals (i.e., utilizing both the data shown in Figures 4 and 5 and intermediate altitude ranges, with overlap between them). We retain this scheme of overlapping altitude bins for the other data shown in Figure 6, to provide a clearer view of the variations with altitude. Meanwhile, the solid green line in Figure 6a shows the magnitude of the draped magnetic field B_D as a function of altitude. Both values can be seen to decrease slowly with altitude, with an approximately constant difference between them over the measured interval, such that $B_D \approx B_T + 18.8 \pm 1.1$ nT. The variations in B_T and B_D with

altitude are fitted using a scale height model, with the resulting fits shown by the dashed lines in Figure 6a. Specifically, the functions

$$B_T(h) = B_{T0} \exp\left(-\frac{h - h_0}{H_T}\right), \tag{6a}$$

and

$$B_D(h) = B_{D0} \exp\left(-\frac{h - h_0}{H_D}\right), \tag{6b}$$

are fitted to the respective measured values using least squares, and values of $B_{T0} = 7.31 \pm 0.29$ nT, $B_{D0} = 26.9 \pm 0.31$ nT, $H_T = 826 \pm 71$ km, and $H_D = 2930 \pm 210$ km are found (h_0 = 325 km, in common with previous expressions).

In Figure 6b we show the linear correlation coefficient computed between the magnetic field modeled by *Cain et al.* [2003] and that measured by MARSIS AIS as the solid black curve. At the lowest altitudes sampled in situ by MEX, the correlation between these two parameters is high, peaking at ~0.9, unsurprisingly indicating that crustal sources contribute significantly to the measured magnetic field at altitudes below ~600 km. The magnitude of this correlation then decreases with altitude as the field configuration becomes closer to that of a typical draped magnetosphere. Meanwhile, the solid red curve in Figure 6b shows the linear correlation between the computed values of V_{n_e} and the measured magnetic field B_M, the value of which is again (to first order) decreasing with increasing altitude. The blue trace then shows the linear correlation between V_{n_e} and the *Cain et al.* [2003] modeled magnetic field, which remains approximately constant across all altitudes (as the location of the observed relative density enhancements remains approximately static). The generally rather low apparent correlation (values of 0.4 to 0.5) between these parameters at the lower altitudes studied suggests that the presence of the Martian crustal fields accounts for only a minor fraction of the overall dependant variation in density, perhaps ~10–20%, underpinning the highly dynamic nature of the Martian ionosphere at these altitudes.

Figure 6c then shows the ratio between the mean values of V_{n_e} recorded in the strong and weak field regions with $|B_{\text{Cain}}| > B_T$ and $|B_{\text{Cain}}| < B_T$ shown by the red and blue lines respectively, and the average value of V_{n_e} computed over the whole surface irrespective of the local crustal field strength, shown by the black line. Appropriately colored shaded regions indicate the standard error on the mean of these quantities, determined in each bin. The red curve, which remains of positive sign at all altitudes, clearly indicates that the enhancement in densities relative to the average in regions with $|B_{\text{Cain}}| > B_T$ is a persistent effect. Meanwhile, the blue curve is of negative sign at all altitudes, indicating measured densities consistently below average. To investigate the significance of this, in Figure 6d we plot the difference between mean density differences V_{n_e} recorded in the strong and weak field regions (red and blue traces in Figure 6c, scaled by the combined standard deviation in their values). The quantity plotted therefore shows the magnitude of the control of the plasma density by the crustal fields. It is equivalent to the result of a Student's *t* test, indicating the confidence of a difference between these two parameters, expressed in units of their joint variability. So expressed, the effect of the crustal fields in establishing the observed pattern of densities is clearly evident at all altitudes sampled, though the significance of the effect decreases by almost a factor of ~2 from ~350 km to ~1200 km (over which the density itself will fall by ~3 orders of magnitude).

The overall picture presented in Figure 6 is therefore one in which the influence of crustal fields is diminished with increasing altitudes, owing to the more rapid decrease of their intensity with altitude relative to the more significant draped IMF. Consequently, the correlation between the measured and modeled magnetic fields drops with altitude, as does the correspondence between the plasma density variations and the measured magnetic field. However, the correlation between the observed density variations and the modeled crustal fields is persistent across all altitudes, in clear agreement with the results presented in Figures 4 and 5.

4. Revised Model

In this section we provide a revised empirical parameterization of the plasma densities sampled in situ by MEX, grouped according to crustal field strength, following a similar approach to that used previously by N11. In Figures 7a–7c we plot observed median plasma densities in the same format used in Figure 2, binned

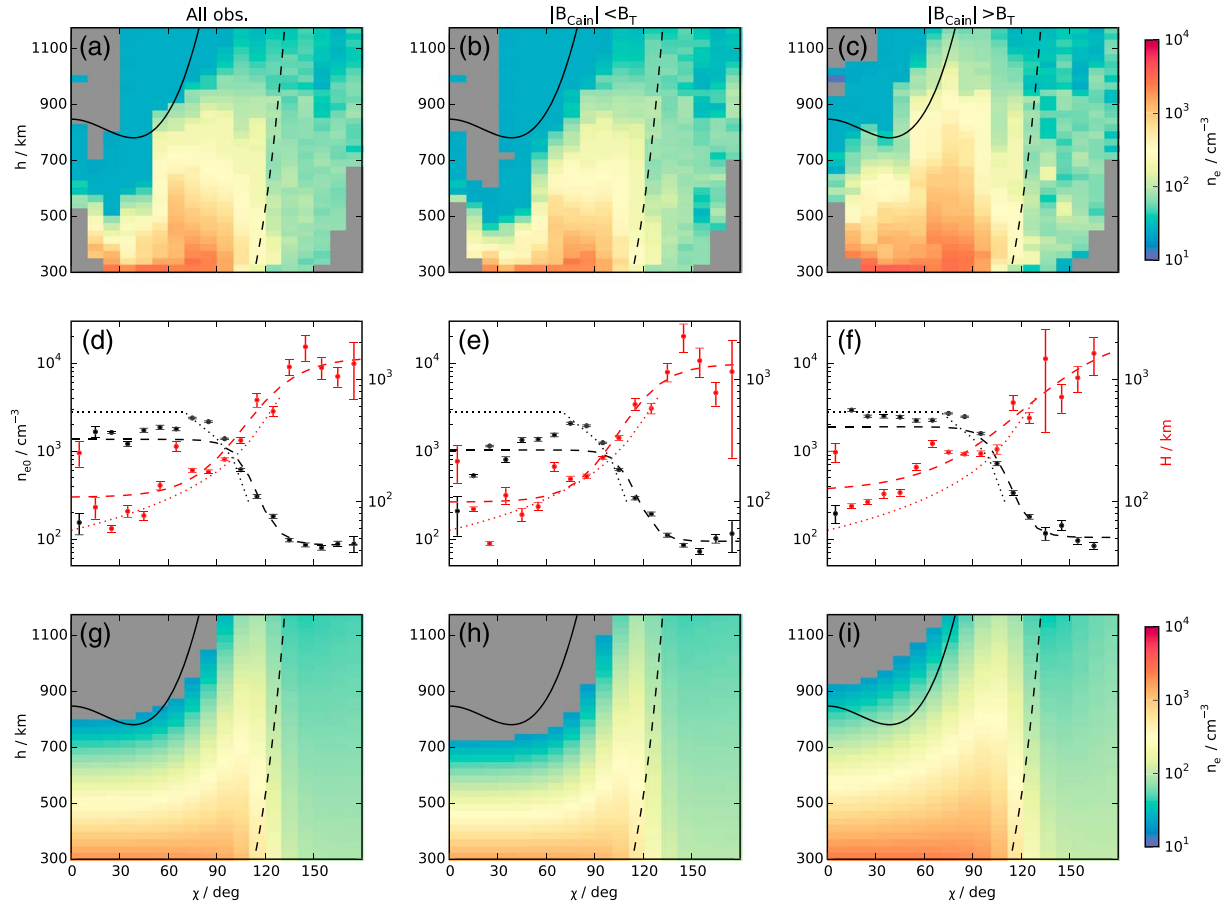

Figure 7. (a–c) Measured median plasma densities from MARSIS, binned by altitude and solar zenith angle using the same scheme as Figure 2. From left to right, Figure 7a shows all available measurements, Figure 7b shows only those for which the modeled crustal magnetic field at the point of each density measurement was less than B_T, while Figure 7c shows only those for which the modeled crustal field was greater than B_T. Solid and dashed lines indicate the modeled positions of the MPB and the terminator, respectively. (d–f) Computed equilibrium densities n_{e0} (black points, left axis) and scale heights H (red points, right axis) versus solar zenith angle, derived in each case from each column in the panels above. Our numerical fits to the data are shown by the appropriately colored dashed lines, while dotted lines show those obtained by N11. (g–i) Empirical density models constituted from the fits shown in Figures 7d–7f, respectively.

versus h and χ. Figure 7a shows the totality of the available data, while Figures 7b and 7c show the median plasma densities recorded at locations where the local value of the *Cain et al.* [2003] model is, respectively, less than or greater than the threshold value B_T at each altitude, as shown in Figure 6. This is then somewhat similar to the results presented previously by *Andrews et al.* [2013], excepting in that here we apply a much more rigorous separation of the measurements based on the expected contribution of crustal sources to the total magnetic field.

The equilibrium plasma density at a given altitude and solar zenith angle $n_e(h, \chi)$ is expressed by the same exponential dependence used by N11,

$$n_e(h, \chi) = n_{e0}(\chi) \exp\left(-\frac{h - h_0}{H(\chi)}\right), \tag{7}$$

in which both the intercept density n_{e0} at $h = h_0 = 325$ km and the scale height H are solely functions of χ. The reference surface for the density h_0 is taken to be 325 km to provide commonality with that used by N11. This parameterization scheme allows us to first fit exponential profiles to the observed densities within the discrete intervals of χ used in constructing Figures 7a–7c (i.e., separate fits are performed to each 10° wide density "column" shown in Figures 7a–7c, using a standard least squares method). The fitted values of n_{e0} and H are shown in Figures 7d–7f, as black and red points, respectively. Error bars indicate 1 σ confidence intervals for the determined parameters. For comparison, we also show the functional forms of the density and scale height dependence used in the N11 model (equations (3b) and (3c)) as appropriately colored dotted lines, which are identical in each panel.

Table 1. Fitted Values of the Parameters in Equations (8a) and (8b)

	α	β	χ_w/deg^{-1}	χ_0/deg^{-1}
		$n_{e0}(\chi)$ *Parameters*		
All	2.54 ± 0.0822	0.6 ± 0.0887	14.6 ± 9.97	115.0 ± 5.73
$B_{Cain}(h) < B_T(h)$	2.5 ± 0.0727	0.519 ± 0.0778	13.4 ± 9.72	116.0 ± 5.57
$B_{Cain}(h) > B_T(h)$	2.65 ± 0.0948	0.628 ± 0.103	14.9 ± 10.4	112.0 ± 6.01
		$H(\chi)$ *Parameters*		
All	2.61 ± 0.0736	−0.572 ± 0.098	34.3 ± 15.4	107.0 ± 8.28
$B_{Cain}(h) < B_T(h)$	2.56 ± 0.0642	−0.565 ± 0.0803	28.9 ± 12.4	105.0 ± 6.84
$B_{Cain}(h) > B_T(h)$	2.75 ± 0.273	−0.664 ± 0.378	61.3 ± 44.7	121.0 ± 30.7

Beginning with the determined intercept densities n_{e0}, when considering the totality of the data available (Figure 7a), these are seen to have approximately constant values of ~2000 cm^{-3} on the dayside (χ less than ~90°, ignoring the poorly determined value closest to the subsolar line). The determined values then fall rapidly across the terminator before once again reaching an approximately constant ~90 cm^{-3} in the deep nightside ($\chi > 135°$). Meanwhile, the fitted scale heights H vary in an opposite manner with χ, being of the order of a few hundred kilometers on the dayside, rising across the terminator and reaching values of the order of 1000 km on the nightside. These nightside scale heights, being comparable to the vertical extent of the entire region, indicate essentially densities which are independent of altitude.

Considering now the intercept densities and scale heights determined in regions of weaker and stronger crustal fields, shown in Figures 7e and 7f, the same general trends are observed with increasing χ in each case. Dayside values of n_{e0} in the strong field region (f) are systematically larger than in the counterpart weak field region (e), as are the scale heights (though to a lesser degree). Cumulatively, these two effects yield densities which are consistently elevated on the dayside in regions where the crustal field is significant, as shown previously in Figures 3 and 4.

In order to provide a simple parameterization of these results, we have elected to fit hyperbolic tangent functions of χ to the logarithms of the determined values of n_{e0} and H. Specifically, we fit the following two functions:

$$\log_{10}(n_{e0}/\mathrm{cm}^{-3}) = \alpha_n + \beta_n \tanh\left(-\frac{\chi - \chi_{0n}}{\chi_{wn}}\right), \tag{8a}$$

and

$$\log_{10}(H/\mathrm{km}) = \alpha_H + \beta_H \tanh\left(-\frac{\chi - \chi_{0H}}{\chi_{wH}}\right), \tag{8b}$$

to each of the two series. The parameters α_k and β_k are dimensionless and define a baseline value of each parameter and the limiting amplitude of its variation with χ, respectively, with appropriate subscripts ($k = n$ or $k = H$) indicating the quantity being fitted. The values of χ_{0k} and χ_{wk} meanwhile specify the central point of the variation with χ, and the width over which it takes place. There is no physical basis for the use of such a function—it is selected as it provides a smooth transition between constant values. Optimal values for the four parameters in each of equations (8a) and (8b) are obtained via a simple least squares fitting procedure to the determined values of n_{e0} and H at each range of χ sampled. These optimal values and their associated uncertainties are given in Table 1. The resulting fitted functions are shown by the appropriately colored dashed lines in Figures 7d–7f. These can be directly compared to the appropriate parameters of the N11 model, described by equations (3b) and (3c).

The scale heights parameterized by equation (8b) can, with the reasonable assumption of a single ion composition (O^+, valid at altitudes above ~200 km), be related to the ion temperature (assuming it is itself constant with altitude). Temperatures so derived range from 1300 to 1500 K, somewhat lower than the ~2800 K reported by N11, owing to the generally larger scale heights obtained in our analysis at the subsolar point.

Finally, the resulting parameterized ionospheric plasma densities are shown color coded versus both altitude and solar zenith angles in Figures 7g–7i, such that they can be directly compared to the observations in Figures 7a–7c. The overall variation in the density is well reproduced in each case, although the

simplified parameterization scheme used clearly prevents the model resolving some of the apparent density variation with χ on the dayside. However, it could well be the case that at least some of the smaller-scale density variation can arise from sampling biases, still present to a small degree even after nearly 10 years of MARSIS operations and therefore should not be expected to be matched by a simple model such as this.

5. Summary and Discussion

In this paper we have further examined the interaction between the Martian ionosphere, the solar wind, and the presence of crustal magnetic field sources. By studying local thermal electron plasma density measurements obtained with MARSIS, comparing values recorded to an existing empirical model of the diffusive plasma equilibrium [*Němec et al.*, 2011], we have shown that the configuration of the ionosphere varies substantially with position over the Martian surface. Plasma densities measured above the strongest crustal field sources are generally elevated above their average values at all altitudes sampled, from ~300 to ~1200 km. This effect persists throughout the entire altitude range, even as the plasma density falls by ~3 orders of magnitude and the crustal fields become significantly weaker relative to the draped interplanetary magnetic field. At these altitudes the ionospheric plasma is expected to be in diffusive equilibrium, with local sources of ionization playing only a very minor role under typical conditions. The density profile is well described by a simple scale height dependence, with the scale height being a smoothly varying function of solar zenith angle.

We note that we have not investigated any seasonal variation in the control of the ionospheric plasma densities, instead expecting the majority of this variation to be averaged out by the long duration of this study. It is conceivable that at least some of the apparent smaller-scale variations in plasma density are the result of seasonal biases remaining in the data, particularly in those regions close to the subsolar and antisolar lines, which are relatively poorly sampled, despite the large overall volume of data used in this study. While the influence of changing insolation on the Martian ionosphere has been investigated at altitudes close to the ionospheric peak [e.g., *Morgan et al.*, 2008; *Němec et al.*, 2011], a full investigation of the seasonal variation in the plasma density in the Martian high-altitude ionosphere remains to be undertaken. Similarly, due in part to a lack of comprehensive simultaneous upstream measurements of the undisturbed solar wind, this study has not investigated the extent to which the apparent organization of the high-altitude ionosphere by the crustal field may be influenced by changing solar wind conditions. Nevertheless, the observation made here that only a small fraction, perhaps ~10–20%, of the total variation associated with the crustal fields is clearly indicative of the large effects that both seasonal and shorter-term variations associated with driving conditions in the solar wind have on this part of the ionosphere.

We tentatively suggest that the large systematic variations in plasma density associated with the local crustal magnetic field strength, within the altitudes studied here, occur as a direct result of the influence of these crustal fields on the local magnetic field structure. At altitudes close to the peak ionospheric plasma density the plasma beta greatly exceeds unity, based on what is currently somewhat limited knowledge of the ionospheric plasma temperature. Nevertheless, a few scale heights above the peak, the plasma beta drops along with the plasma density, falling below unity and indicating that the crustal and draped magnetic fields are able to dictate, to an increasing extent, the distribution of plasma. In regions where the crustal fields are significant compared to the near-horizontal (low-inclination) draped interplanetary magnetic field, they act to distort the picture of a typical draped magnetosphere, giving field configurations which are on average less horizontal. This change in field inclination modifies the efficacy of both vertical and horizontal transport of ionospheric plasma (in this region where the local ionization rates are insignificant) and consequently allows higher equilibrium densities to be present at higher altitudes in the former case and allows enhanced transterminator plasma flows in the latter case, populating the nightside ionosphere. In comparing to the N11 model, which represents the "average" conditions of the dayside ionosphere, local enhancements in the plasma density in regions of strong crustal fields are balanced elsewhere by local reductions relative to the model value.

As noted in section 1, several previous studies have related the position of the magnetic pileup boundary (variously also termed the "magnetic boundary" and the "induced magnetospheric boundary") to the presence of intense crustal field sources. *Crider et al.* [2002] provided initial evidence that the altitude of the MPB depended on latitude, being higher in the southern hemisphere where the crustal fields are on average more intense. Later studies showed an explicit dependence of the MPB and BS altitudes on the intensities

of the crustal fields at lower altitudes [*Edberg et al.*, 2008, 2009]. The shapes and locations of these boundaries are dictated by the balance of magnetic, thermal, and dynamic pressures, and under the assumption of a constant plasma temperature the enhanced plasma densities over crustal fields will likely contribute to the elevation of the plasma boundaries. In this sense, the results presented in this paper are consistent with these previous observations, though we note that the thermal plasma pressure only contributes weakly to the total; i.e., the magnetic pressure exerted by the induced magnetic field is by far the dominant term, as found previously, e.g., by *Dubinin et al.* [2008]. Plasma temperatures derived from the density scale heights, as in this study, are likely to be inaccurate owing to the isothermal assumption involved. Therefore, while the "true" temperature could conceivably be significantly higher than the ~1300-1500 K estimated here, in order for the ionospheric thermal pressure to play a major role in establishing the structure of these boundaries, this value would need to be increased by more than an order of magnitude at the interface. Likewise, as shown in this study, the averaged induced magnetic fields clearly dominate over the crustal sources at high altitudes (Figure 6a), again indicating that the contribution of the crustal fields to the total magnetic pressure is typically the smaller of the two. We anticipate future studies that will investigate this issue in more detail. In addition, both the MPB and BS have been shown to be highly dynamic, rapidly responding to changes in the upstream solar wind, and in this respect, having high-cadence and near-simultaneous measurements of both the upstream solar wind and the state of the ionosphere may be a necessary next step in furthering understanding of this interaction, and how the influence of these crustal fields is exerted at such high altitudes.

Further studies have shown that the ionopause (specifically, rapid decreases in ionospheric density with altitude over and above the typical quasi-exponential dependence presented here) is also influenced by the presence of intense crustal magnetic field sources. Defining a crossing of the ionopause as a drop in density of at least 300 cm^{-3} over not more than five successive AIS soundings (~40 s, or ~30 km in altitude for a typical MEX orbit), *Duru et al.* [2009] found that such crossings were often observed at higher altitudes over strong crustal fields, with the shift in altitude being as much as ~100 km. However, as sharp density gradients such as these are somewhat rare features (observed only on ~8% of orbits), we do not further comment on this phenomenon in relation to our observations of the long-term average state of the ionosphere. Observations of such sharp vertical density gradients are likewise relatively rare in radio occultation measurements [see, e.g., *Schunk and Nagy*, 2004; *Duru et al.*, 2009; *Witasse et al.*, 2008].

In the interests of allowing simple comparisons to be made against this data set, we provide a revised parameterization of the observed ionospheric plasma density in the 300 to 1200 km altitude range, described wholly by equations (7) and (8) and the values given in Table 1. The exponential fit to the crustal field threshold value B_T expressed in equation (6a) can be used to conveniently distinguish between the "weak" and "strong" crustal field regimes. We use purely empirical functions to describe the dependence of the density and scale height on solar zenith angle. However, it is worth recalling that at lower altitudes, closer to the ionospheric peak, the density follows $\cos(\chi)^{1/2}$, thereby varying more slowly with χ near the subsolar point than at the terminator and therefore not dissimilar to the hyperbolic tangent we use to replicate this behavior at higher altitudes (where the terminator is anyway found at larger values of χ). We anticipate that the usefulness of this parameterization is found in providing an easily calculated reasonable estimate for the plasma densities in this altitude range, in both regions where the crustal fields are insignificant, and regions in which they dominate.

Finally, we briefly comment on the presented measurements of magnetic fields. First, we note that those estimates of the intensities of the dayside-averaged draped magnetic field B_D are in good agreement with values reported from MGS observations [*Brain et al.*, 2003; *Crider et al.*, 2004]. Considering the expressions for B_T and B_D given by equations (6a) and (6b), if we take the crustal field expressed by B_T to be pure radial and the draped field B_D to be pure horizontal, we obtain an expression for the upper limit of the magnetic field inclination $\tan I = B_T/B_D$, which decreases exponentially with altitude from ~20° at $h = 300$ km to ~3° at $h = 1200$ km. As this is an upper limit, this nevertheless suggests that significant modification of the ionospheric plasma density is present in regions where the deflection of the draped magnetic field by the crustal fields is likely to be rather small. *Brain et al.* [2003] further quantified the interaction between the crustal and draped fields by defining a "transition altitude" by inspecting radial profiles of MGS measured magnetic fields obtained during the premapping orbits, locating the altitude at which the field ceases to be well-described by a power law with exponent less than −2 (as is the case for an infinitely long magnetized cylinder at the surface; more complex or higher-order fields will decrease in strength even faster with

altitude.) *Brain et al.* [2003] found that this altitude was essentially indeterminate in regions of weak crustal fields but reached a maximum of ~1400 km at the location of the most intense sources. Typical transition altitudes over the regions of the planet's surface for which we here observe elevated ionospheric electron densities are ~700–1200 km [e.g., *Brain et al.*, 2003, Figure 11].

In conclusion, it seems apparent that there remains more to be understood regarding the precise mechanism of the interaction between the Martian ionosphere, crustal fields, and solar winds. With the new availability of measurements from the Mars Atmosphere and Volatile Evolution Mission (MAVEN) spacecraft, in particular in respect to higher-cadence measurements of the ionospheric electron density and temperature by the Langmuir probe and waves instrument, we are hopeful that significant progress can be made on this topic.

Acknowledgments

D.J.A., H.J.O., M.A., and N.J.T.E. acknowledge funding from the Swedish National Space Board. F.N. was supported by the KONTAKT II grant LH13031. Data used in this study are available via the ESA Planetary Science Archive, http://www.rssd.esa.int/PSA.

Michael Liemohn thanks the reviewers for their assistance in evaluating this paper.

References

Acuña, M., et al. (1998), Magnetic field and plasma observations at Mars: Initial results of the Mars Global Surveyor Mission, *Science*, *279*(5357), 1676–1680.

Acuña, M., et al. (1999), Global distribution of crustal magnetization discovered by the Mars Global Surveyor MAG/ER experiment, *Science*, *284*(5415), 790–793.

Acuña, M. H., et al. (2001), Magnetic field of Mars: Summary of results from the aerobraking and mapping orbits, *J. Geophys. Res.*, *106*, 23,403–23,418, doi:10.1029/2000JE001404.

Andrews, D. J., H. J. Opgenoorth, N. J. T. Edberg, M. André, M. Fränz, E. Dubinin, F. Duru, D. Morgan, and O. Witasse (2013), Determination of local plasma densities with the MARSIS radar: Asymmetries in the high-altitude Martian ionosphere, *J. Geophys. Res. Space Physics*, *118*, 6188–6196, doi:10.1002/jgra.50593.

Andrews, D. J., M. André, H. J. Opgenoorth, N. J. T. Edberg, C. Diéval, F. Duru, D. A. Gurnett, D. Morgan, and O. Witasse (2014), Oblique reflections in the Mars Express MARSIS data set: Stable density structures in the Martian ionosphere, *J. Geophys. Res. Space Physics*, *119*, 3944–3960, doi:10.1002/2013JA019697.

Arkani-Hamed, J. (2001), A 50-degree spherical harmonic model of the magnetic field of Mars, *J. Geophys. Res.*, *106*, 23,197–23,208, doi:10.1029/2000JE001365.

Arkani-Hamed, J. (2004), A coherent model of the crustal magnetic field of Mars, *J. Geophys. Res.*, *109*, E09005, doi:10.1029/2004JE002265.

Barabash, S., et al. (2006), The Analyzer of Space Plasmas and Energetic Atoms (ASPERA-3) for the Mars express mission, *Space Sci. Rev.*, *126*, 113–164, doi:10.1007/s11214-006-9124-8.

Brain, D. A., F. Bagenal, M. H. Acuña, and J. E. P. Connerney (2003), Martian magnetic morphology: Contributions from the solar wind and crust, *J. Geophys. Res.*, *108*, 1424, doi:10.1029/2002JA009482.

Brecht, S. H., and S. A. Ledvina (2014), The role of the Martian crustal magnetic fields in controlling ionospheric loss, *Geophys. Res. Lett.*, *41*, 5340–5346, doi:10.1002/2014GL060841.

Cain, J. C., B. B. Ferguson, and D. Mozzoni (2003), An $n = 90$ internal potential function of the Martian crustal magnetic field, *J. Geophys. Res.*, *108*, 5008, doi:10.1029/2000JE001487.

Chicarro, A., P. Martin, and R. Trautner (2004), The Mars Express mission: An overview, in *Mars Express: The Scientific Payload*, edited by A. Wilson and A. Chicarro, *ESA Spec. Publ., 1240*, 3–13.

Connerney, J. E. P., M. H. Acuna, P. J. Wasilewski, N. F. Ness, H. Reme, C. Mazelle, D. Vignes, R. P. Lin, D. L. Mitchell, and P. A. Cloutier (1999), Magnetic lineations in the ancient crust of Mars, *Science*, *284*, 794, doi:10.1126/science.284.5415.794.

Connerney, J. E. P., M. H. Acuña, P. J. Wasilewski, G. Kletetschka, N. F. Ness, H. Rème, R. P. Lin, and D. L. Mitchell (2001), The global magnetic field of Mars and implications for crustal evolution, *Geophys. Res. Lett.*, *28*, 4015–4018, doi:10.1029/2001GL013619.

Crider, D. H., et al. (2002), Observations of the latitude dependence of the location of the Martian magnetic pileup boundary, *Geophys. Res. Lett.*, *29*(8), 1170, doi:10.1029/2001GL013860.

Crider, D. H., D. A. Brain, M. H. Acuña, D. Vignes, C. Mazelle, and C. Bertucci (2004), Mars global surveyor observations of solar wind magnetic field draping around Mars, *Space Sci. Rev.*, *111*, 203–221, doi:10.1023/B:SPAC.0000032714.66124.4e.

Crider, D. H., J. Espley, D. A. Brain, D. L. Mitchell, J. E. P. Connerney, and M. H. Acuña (2005), Mars Global Surveyor observations of the Halloween 2003 solar superstorm's encounter with Mars, *J. Geophys. Res.*, *110*, A09S21, doi:10.1029/2004JA010881.

Dong, C., S. W. Bougher, Y. Ma, G. Toth, A. F. Nagy, and D. Najib (2014), Solar wind interaction with Mars upper atmosphere: Results from the one-way coupling between the multifluid MHD model and the MTGCM model, *Geophys. Res. Lett.*, *41*, 2708–2715, doi:10.1002/2014GL059515.

Dubinin, E., et al. (2008), Plasma environment of Mars as observed by simultaneous MEX-ASPERA-3 and MEX-MARSIS observations, *J. Geophys. Res.*, *113*, A10217, doi:10.1029/2008JA013355.

Dubinin, E., M. Fränz, J. Woch, G. Chanteur, F. Duru, D. A. Gurnett, S. Barabash, and R. Lundin (2012), Upper atmosphere of Mars is not axially symmetrical, *Earth Planets Space*, *64*, 113–120, doi:10.5047/eps.2011.05.022.

Duru, F., D. A. Gurnett, T. F. Averkamp, D. L. Kirchner, R. L. Huff, A. M. Persoon, J. J. Plaut, and G. Picardi (2006), Magnetically controlled structures in the ionosphere of Mars, *J. Geophys. Res.*, *111*, A12204, doi:10.1029/2006JA011975.

Duru, F., D. A. Gurnett, D. D. Morgan, R. Modolo, A. F. Nagy, and D. Najib (2008), Electron densities in the upper ionosphere of Mars from the excitation of electron plasma oscillations, *J. Geophys. Res.*, *113*, A07302, doi:10.1029/2008JA013073.

Duru, F., D. A. Gurnett, R. A. Frahm, J. D. Winningham, D. D. Morgan, and G. G. Howes (2009), Steep, transient density gradients in the Martian ionosphere similar to the ionopause at Venus, *J. Geophys. Res.*, *114*, A12310, doi:10.1029/2009JA014711.

Edberg, N. J. T., M. Lester, S. W. H. Cowley, and A. I. Eriksson (2008), Statistical analysis of the location of the Martian magnetic pileup boundary and bow shock and the influence of crustal magnetic fields, *J. Geophys. Res.*, *113*, A08206, doi:10.1029/2008JA013096.

Edberg, N. J. T., D. A. Brain, M. Lester, S. W. H. Cowley, R. Modolo, M. Fränz, and S. Barabash (2009), Plasma boundary variability at Mars as observed by Mars Global Surveyor and Mars Express, *Ann. Geophys.*, *27*, 3537–3550, doi:10.5194/angeo-27-3537-2009.

Gurnett, D. A., et al. (2005), Radar soundings of the ionosphere of Mars, *Science*, *310*, 1929–1933, doi:10.1126/science.1121868.

Gurnett, D. A., et al. (2008), An overview of radar soundings of the Martian ionosphere from the Mars Express spacecraft, *Adv. Space Res.*, *41*, 1335–1346, doi:10.1016/j.asr.2007.01.062.

Haider, S. A., K. K. Mahajan, and E. Kallio (2011), Mars ionosphere: A review of experimental results and modeling studies, *Rev. Geophys.*, *49*, RG4001, doi:10.1029/2011RG000357.
Harnett, E. M., and R. M. Winglee (2003), The influence of a mini-magnetopause on the magnetic pileup boundary at Mars, *Geophys. Res. Lett.G*, *30*(20), 2074, doi:10.1029/2003GL017852.
Harnett, E. M., and R. M. Winglee (2005), Three-dimensional fluid simulations of plasma asymmetries in the Martian magnetotail caused by the magnetic anomalies, *J. Geophys. Res.*, *110*, A07226, doi:10.1029/2003JA010315.
Harnett, E. M., and R. M. Winglee (2007), High-resolution multifluid simulations of the plasma environment near the Martian magnetic anomalies, *J. Geophys. Res.*, *112*, A05207, doi:10.1029/2006JA012001.
Jordan, R., et al. (2009), The Mars express MARSIS sounder instrument, *Planet. Space. Sci.*, *57*, 1975–1986, doi:10.1016/j.pss.2009.09.016.
Lillis, R. J., M. E. Purucker, J. S. Halekas, K. L. Louzada, S. T. Stewart-Mukhopadhyay, M. Manga, and H. V. Frey (2010), Study of impact demagnetization at Mars using Monte Carlo modeling and multiple altitude data, *J. Geophys. Res.*, *115*, E07007, doi:10.1029/2009JE003556.
Lundin, R., S. Barabash, M. Holmström, H. Nilsson, Y. Futaana, R. Ramstad, M. Yamauchi, E. Dubinin, and M. Fraenz (2013), Solar cycle effects on the ion escape from Mars, *Geophys. Res. Lett.*, *40*, 6028–6032, doi:10.1002/2013GL058154.
Ma, Y., A. F. Nagy, K. C. Hansen, D. L. DeZeeuw, T. I. Gombosi, and K. G. Powell (2002), Three-dimensional multispecies MHD studies of the solar wind interaction with Mars in the presence of crustal fields, *J. Geophys. Res.*, *107*, 1282, doi:10.1029/2002JA009293.
Ma, Y., A. F. Nagy, I. V. Sokolov, and K. C. Hansen (2004), Three-dimensional, multispecies, high spatial resolution MHD studies of the solar wind interaction with Mars, *J. Geophys. Res.*, *109*, A07211, doi:10.1029/2003JA010367.
Ma, Y., X. Fang, A. F. Nagy, C. Russell, and G. Toth (2014), Martian ionospheric responses to dynamic pressure enhancements in the solar wind, *J. Geophys. Res. Space Physics*, *119*, 1272–1286, doi:10.1002/2013JA019402.
Ma, Y.-J., and A. F. Nagy (2007), Ion escape fluxes from Mars, *Geophys. Res. Lett.*, *340*, L08201, doi:10.1029/2006GL029208.
Morgan, D., O. Witasse, E. Nielsen, D. Gurnett, F. Duru, and D. Kirchner (2013), The processing of electron density profiles from the Mars Express MARSIS topside sounder, *Radio Sci.*, *48*(3), 197–207, doi:10.1002/rds.20023.
Morgan, D. D., D. A. Gurnett, D. L. Kirchner, J. L. Fox, E. Nielsen, and J. J. Plaut (2008), Variation of the Martian ionospheric electron density from Mars Express radar soundings, *J. Geophys. Res.*, *113*, A09303, doi:10.1029/2008JA013313.
Morschhauser, A., V. Lesur, and M. Grott (2014), A spherical harmonic model of the lithospheric magnetic field of Mars, *J. Geophys. Res. Planets*, *119*, 1162–1188, doi:10.1002/2013JE004555.
Nagy, A. F., et al. (2004), The plasma environment of Mars, *Space Sci. Rev.*, *111*, 33–114, doi:10.1023/B:SPAC.0000032718.47512.92.
Najib, D., A. F. Nagy, G. Tóth, and Y. Ma (2011), Three-dimensional, multifluid, high spatial resolution MHD model studies of the solar wind interaction with Mars, *J. Geophys. Res.*, *116*, A05204, doi:10.1029/2010JA016272.
Nielsen, E., X.-D. Wang, D. A. Gurnett, D. L. Kirchner, R. Huff, R. Orosei, A. Safaeinili, J. J. Plaut, and G. Picardi (2007), Vertical sheets of dense plasma in the topside Martian ionosphere, *J. Geophys. Res.*, *112*, E02003, doi:10.1029/2006JE002723.
Nilsson, H., N. J. T. Edberg, G. Stenberg, S. Barabash, M. Holmström, Y. Futaana, R. Lundin, and A. Fedorov (2011), Heavy ion escape from Mars, influence from solar wind conditions and crustal magnetic fields, *Icarus*, *215*, 475–484, doi:10.1016/j.icarus.2011.08.003.
Němec, F., D. D. Morgan, D. A. Gurnett, F. Duru, and V. Truhlík (2011), Dayside ionosphere of Mars: Empirical model based on data from the MARSIS instrument, *J. Geophys. Res.*, *116*, E07003, doi:10.1029/2010JE003789.
Picardi, G., et al. (2004), MARSIS: Mars Advanced Radar for Subsurface and Ionosphere Sounding, in *Mars Express: The Scientific Payload*, edited by A. Wilson and A. Chicarro, *ESA Spec. Publ., 1240*, 51–69.
Purucker, M., D. Ravat, H. Frey, C. Voorhies, T. Sabaka, and M. Acuña (2000), An altitude-normalized magnetic map of Mars and its interpretation, *Geophys. Res. Lett.*, *27*, 2449–2452, doi:10.1029/2000GL000072.
Schunk, R. W., and A. F. Nagy (2004), *Ionospheres*, Cambridge Univ. Press, Cambridge, U. K.
Trotignon, J. G., C. Mazelle, C. Bertucci, and M. H. Acuña (2006), Martian shock and magnetic pile-up boundary positions and shapes determined from the Phobos 2 and Mars Global Surveyor data sets, *Planet. Space. Sci.*, *54*, 357–369, doi:10.1016/j.pss.2006.01.003.
Witasse, O., T. Cravens, M. Mendillo, J. Moses, A. Kliore, A. Nagy, and T. Breus (2008), Solar system ionospheres, *Space Sci. Rev.*, *139*, 235–265, doi:10.1007/s11214-008-9395-3.
Withers, P. (2009), A review of observed variability in the dayside ionosphere of Mars, *Adv. Space Res.*, *44*, 277–307, doi:10.1016/j.asr.2009.04.027.